

Light scattering observation of oscillation of a bubble in acoustic cavitation cloud

Takanobu Kuroyama¹

¹ National Institute of Technology, Gifu College, Japan

ABSTRACT

High-intensity ultrasound in liquid generates oscillating fine bubbles called acoustic cavitation. Although the behavior of the oscillation of the single bubbled driven by ultrasound is revealed, the behavior of the bubbles in the multi-bubble system is not clear because of the difficulty of the measurement. To overcome the problem, we propose an improved light scattering measurement technique employing confocal optics. In this system, a laser beam irradiates the bubble cloud. The light scattered by a bubble in a tiny measurement volume, which is formed by the confocal optics, is measured. The detected scattered light intensity is proportional to the square of the bubble diameter. Thus, the oscillation of a bubble in the cloud can be observed with the scattered light. The concept and the principle of measurement are described and the characteristics are analyzed by numerical simulation. The verification experiment is performed and the oscillation of a bubble in acoustic cavitation formed under the ultrasonic horn is measured. The single bubble oscillation-like behavior of a bubble in the acoustic cavitation is observed and it may indicate the ability of the proposed method to measure the oscillation of a single bubble in the acoustic cavitation.

Keywords: Acoustic cavitation, Oscillation, Laser scattering

1. INTRODUCTION

Acoustic cavitation means a cavitation phenomenon induced by the high-intensity ultrasound in the liquid. The negative pressure of the ultrasound causes the deposition of the dissolved gases in the liquid and the deposited gases form tiny bubbles. These bubbles volumetrically oscillate with the fluctuation of the ultrasound pressure. The bubbles gradually expand with the negative ultrasound pressure and rapidly contract with the positive ultrasound pressure within a ultrasound period even if the bubble is driven by the sinusoidal ultrasound pressure. The shrinkage stage of the bubble accompanies the violent collapse and the semi-adiabatic compression of the inner gas. The collapse of the bubbles produces various chemical and physical phenomena, such as the sonoluminescence (1), sonochemiluminescence (2), production of radicals (3), and microjet (4).

The physics of the above mentioned nonlinear bubble oscillation has been revealed theoretically and experimentally for the single bubble case. Especially, the single bubble oscillation experiment performed by Gaitan and Crum made further understanding of the bubble oscillation (5). In the single bubble oscillation experiment, a bubble is trapped at the antinode of 10¹ kHz order ultrasonic standing wave. The trapped bubble stably oscillates with an accurate period without translational motion. Thus, the bubble oscillation can be easily observed with the stroboscopic imaging (6) or the laser scattering measurement (7, 8). However, the bubble oscillation in acoustic cavitation with multi bubbles is difficult to be observed because the bubbles move randomly. The bubble oscillation in ordinal acoustic cavitation is complicated because the bubbles mutually interact with each other and the formation, coalescence, and collapse of the bubble occur. Thus, the oscillation characteristics of the bubble in the acoustic cavitation are still unclear.

In this paper, we propose a measurement method of the oscillation of a single bubble in acoustic cavitation employing the laser scattering. The purpose of this paper is to establish the measurement principle of the method. First, the concept and the theory of the measurement method are described. The numerical simulation is performed to clarify the characteristics of the proposed method and the result of the experimental observation of the bubble oscillation is discussed.

¹ kuroyama@gifu-nct.ac.jp

2. Measurement Principle

2.1 Concept of Proposed Method

The optical system of the proposed method is shown in Figure 1. Acoustic cavitation bubbles in water are irradiated by a Gaussian laser beam and the bubbles scatter the laser. An imaging lens is positioned so that the image of the side scattered light from bubbles are formed on the pinhole. The output of the photodetector is proportional to the power of the scattered light image on the pinhole aperture. This lens system is called confocal optics. The scattered light only arises when the laser beam crosses the bubbles and the bubble image is formed away from the optical axis of the lens system when the bubble is far from the optical axis. Thus, the photodetector only detects the scattered light when a bubble is positioned in the measurement volume, where the laser beam has high light intensity near the optical axis of the lens system.

The size of the measurement volume, V , is approximated as

$$V \approx [\pi(d/M)^2/4]D, \quad (1)$$

where d , M , D are the pinhole aperture diameter, the magnitude of the lens system, and the laser beam diameter, respectively. Assuming that the bubble is spatially randomly distributed, the number of bubble within the measurement volume k follows the Poisson distribution with a mean number of bubbles in the measurement volume μ denoted as P_k , such that

$$P_k = \frac{\mu^k \exp(-\mu)}{k!}, \quad (2)$$

$$\mu = NV$$

where N is the number density of the bubbles (9). The probability of existing two or more bubbles in the measurement volume can be reduced by decreasing the mean number of bubbles μ . The mean number of bubbles μ can be set to small by reducing the measurement volume.

The side scattered light intensity is almost proportional to the square of the bubble diameter (10). Thus, the radial oscillation of the bubble varies the scattered light intensity. When a single bubble is located in the measurement volume, the radial oscillation can be measured with the fluctuation of the photodetector output.

2.2 Scattering of Gaussian Laser Beam by Bubble in Water

Schematic diagram of coordinates for Gaussian beam scattering is shown in Figure 2. The bubble at origin is irradiated with a Gaussian beam focused to the half-width w_0 at the point (x_f, y_f, z_f) . The far-field intensity of the scattered light is expressed as

$$I(r, \theta, \phi) \propto [|S_1(\theta, \phi)|^2 + |S_2(\theta, \phi)|^2] / r^2, \quad (3)$$

where r , θ , and ϕ are the distance between the bubble center and the origin, the scattering angle, and the angle between the x -axis and the scattering plane as shown in Figure 3, respectively. The scattering function for x -polarized light $S_1(\theta, \phi)$ and for y -polarized light $S_2(\theta, \phi)$ are expressed as

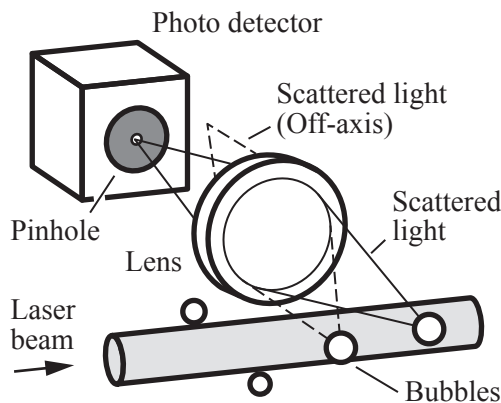


Figure 1 – Concept of proposed method

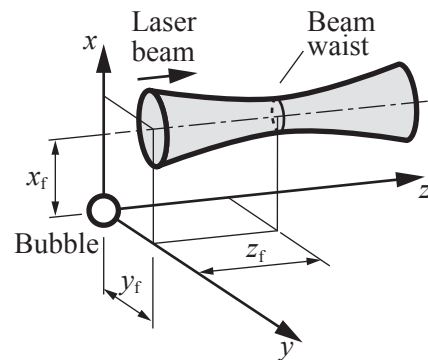


Figure 2 – Gaussian beam scattering coordinates

$$S_1(\boldsymbol{\theta}, \phi) = \sum_{l=1}^{\infty} \sum_{m=-l}^l \frac{2l+1}{2l(l+1)} \left[-jm\alpha_{lm} \pi_l^{(m)}(\boldsymbol{\theta}) + \beta_{lm} \tau_l^{(m)}(\boldsymbol{\theta}) \right] \exp(jm\phi), \quad (4)$$

$$S_2(\boldsymbol{\theta}, \phi) = \sum_{l=1}^{\infty} \sum_{m=-l}^l \frac{2l+1}{2l(l+1)} \left[jm\beta_{lm} \pi_l^{(m)}(\boldsymbol{\theta}) + \alpha_{lm} \tau_l^{(m)}(\boldsymbol{\theta}) \right] \exp(jm\phi), \quad (5)$$

where $\pi_l^{(m)}(\boldsymbol{\theta})$ and $\tau_l^{(m)}(\boldsymbol{\theta})$ are the angular functions. The partial-wave scattering amplitudes α_{lm} and β_{lm} are the function of the beam waist position (x_f, y_f, z_f), half beam diameter w_0 , and the bubble properties, such as the diameter and the refractive index (11).

2.3 Imaging Characteristics of Lens System

The scattered light of the bubble is condensed on the pinhole at the entrance of the photodetector by the imaging lens as shown in Figure 4. The front focal distance l_1 and the back focal distance l_2 satisfy the lens formula $l_1^{-1} + l_2^{-1} = f^{-1}$ where f is the focal length of the lens. The magnitude of the lens system M is calculated as $M = -l_2 / l_1$, where the negative sign means the inversion of the image. The light amplitude on the image plane, which is on the pinhole, becomes the convolution between the apparent light amplitude distribution of the scattered light on the object plane x - z and the amplitude point spread function. Thus, the x -polarized light amplitude on the image plane $c_1(x, z; x_b, y_b, z_b)$ for the scattered light from a bubble located at (x_b, y_b, z_b) is shown as

$$c_1(x, z; x_b, y_b, z_b) = c_1'(x/M, z/M; x_b, y_b, z_b), \quad (6)$$

$$c_1'(x, z; x_b, y_b, z_b) = s_1(x, z; x_b, y_b, z_b) * h(x, z; y_b), \quad (7)$$

where $s_1(x, z; x_b, y_b, z_b)$ is the apparent x -directional light amplitude of the scattered light on the object plane (12). The amplitude point spread function $h(x, z; y_b)$ is given by

$$h(x, z; y_b) = \int_0^1 P(\boldsymbol{\rho}, y_b) J_0\left(k\rho NA \sqrt{x^2 + z^2}\right) \boldsymbol{\rho} d\boldsymbol{\rho}, \quad (8)$$

$$P(\boldsymbol{\rho}, y_b) = \exp[j2y_b kn \sin^2(\boldsymbol{\alpha}/2)\boldsymbol{\rho}^2], \quad (9)$$

$$NA = n \sin(\boldsymbol{\alpha}), \quad (10)$$

$$\tan(\boldsymbol{\alpha}) = (D_L / 2) / l_1, \quad (11)$$

where J_0 , n , $\boldsymbol{\alpha}$, NA , and D_L are the first-kind zeroth-order Bessel function, the refractive index of the medium surrounding the lens, the angle of aperture, the numerical aperture, and the aperture diameter of lens, respectively (13). The optical wavenumber k is given by $k = 2\pi / \lambda$ where λ is the optical wavelength.

2.4 Photodetector Output

The apparent x -polarized light amplitude $s_1(x, z; x_b, y_b, z_b)$ in Eq. 7 can be calculated from the scattering function shown in Eq. 4. The spatial Fourier transformation $S_1'(\boldsymbol{v}_x, \boldsymbol{v}_z)$ of the apparent x -polarized light amplitude for a bubble at origin $s_1'(x, z) = s_1(x, z; 0, 0, 0)$ is given by

$$S_1'(\boldsymbol{v}_x, \boldsymbol{v}_z) = \iint s_1'(x, z) \exp[2\pi(\boldsymbol{v}_x x + \boldsymbol{v}_z z)] dx dz, \quad (12)$$

where \boldsymbol{v}_x and \boldsymbol{v}_z are the x - and z -directional spatial frequency, respectively. The spatial frequencies are related with the propagation angle of the scattered light as (14)

$$\cos(\boldsymbol{\theta}) = \lambda \boldsymbol{v}_z, \quad (13)$$

$$\cos(\boldsymbol{\phi}) = \lambda \boldsymbol{v}_x. \quad (14)$$

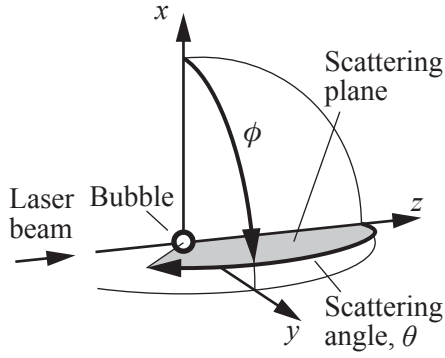


Figure 3 – Scattered light coordinates

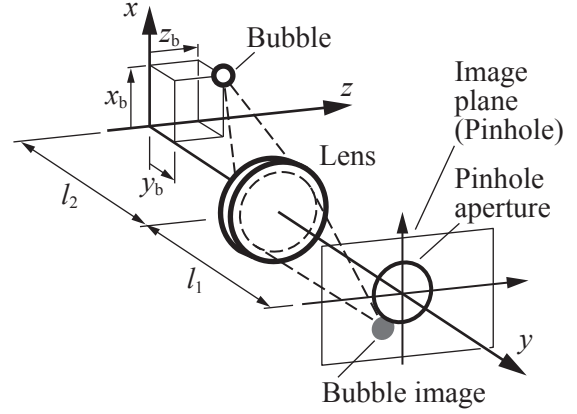


Figure 4 – Imaging coordinates

Therefore, the apparent light amplitude $s_1'(x, z)$ can be obtained by the inverse Fourier transformation of the scattering function by replacing the spatial frequency with the converted propagation angle. When the bubble is located at (x_b, y_b, z_b) , the light amplitude distribution displaces from the origin as $s_1(x, z; x_b, y_b, z_b) = s_1'(x - x_b, z - z_b)$. The y -directional displacement of the bubble y_b does not affect the apparent light amplitude but affects the amplitude point spread function of the lens system. From the definition of the coordinates shown in Figures 2 and 4, the bubble displacement and the beam waist position have a relationship as $x_f = -x_b$, $y_f = -y_b$, and $z_f = -z_b - z_{bw}$ where z_{bw} is the distance between the lens axis and the beam waist position. The power of the x -polarized scattered light passing through the pinhole aperture becomes the integration of the light intensity on the aperture as

$$O_1(x_b, y_b, z_b) = \iint_{(x^2+z^2) < (d/2)^2} |c_1(x, z; x_b, y_b, z_b)|^2 dx dz. \quad (15)$$

Similarly, the power of the y -polarized scattered light passing through the pinhole aperture is expressed as

$$O_2(x_b, y_b, z_b) = \iint_{(x^2+z^2) < (d/2)^2} |c_2(x, z; x_b, y_b, z_b)|^2 dx dz, \quad (16)$$

where $c_2(x, z; x_b, y_b, z_b)$ is the y -polarized light amplitude on the image plane. The output of the photodetector, $O(x_b, y_b, z_b)$, is proportional to the total power as

$$O(x_b, y_b, z_b) \propto O_1(x_b, y_b, z_b) + O_2(x_b, y_b, z_b). \quad (17)$$

3. Simulation of Measurement Property of Optical System

3.1 Experimental Setup of Measurement System

The schematic diagram of the experimental setup is shown in Figure 5. A bolt-clamped Langevin-type transducer (BLT) with a horn radiates ultrasound into the water in a glass vessel with an inner dimension of $40 \times 40 \times 68$ (mm³). The diameter of the horn output surface is 30 mm. The BLT is driven by the sinusoidal voltage with frequency of 19.29 kHz. The acoustic cavitation bubbles as the measurement targets mainly distribute just below the horn surface.

The acoustic cavitation bubbles below the horn are irradiated by a Gaussian laser beam generated by a He-Ne laser source. The beam waist is located at the exit aperture of the laser source and has 0.4 mm of half beam diameter. The distance between the exit aperture and the horn axis is 600 mm. The scattered light from the bubbles enters a lens and the condensed scattered light is measured with an avalanche photodiode module (APD). The front focal length of the lens is 80 mm and the diameter of the lens aperture is 48 mm. The diameter of the active area, which corresponds to the diameter of the pinhole aperture, is 1.5 mm. The magnification of the lens system is 3 and the numerical aperture is 0.287. Thus, the object plane equivalent pinhole diameter $d / |M|$ is 0.5 mm.

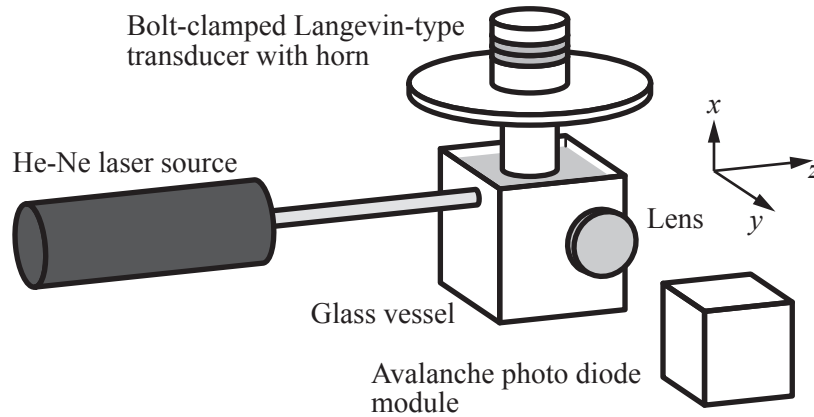


Figure 5 – Experimental setup

The output signal of the APD is recorded via an analog to digital converter (ADC). The sampling frequency of the ADC is 25 MHz. The recorded signal of the APD is band-limited below 10 MHz by the frequency response of the APD. The driving voltage and the current fed to the BLT are simultaneously recorded by the ADC and the driving power is calculated.

3.2 Spatial Sensitivity Characteristics to Bubble Position

Numerical simulation of the photodetector output was performed to reveal the characteristics of the proposed method. The bubble position dependence of the photodetector output for the bubble diameter of $10\ \mu\text{m}$ is shown in Figure 6. The photodetector output is normalized by the maximum value observed in the simulation for the bubble diameter of $10\ \mu\text{m}$. The photodetector output has a large value in the circular region centered at $(x_b, z_b) = (0, 0)$ on $y_b = 0$ plane as shown in Figure 6(a). The diameter of the circular region is almost the same as the object plane equivalent pinhole diameter $d / |M|$. Although the boundary of the region is blurred by the diffraction limit of the lens system and the defocus, the shape of the measurement volume in x_b - z_b cross section is dominated by the shape of the pinhole for any y_b . The output variation along the x_b -axis is caused by the radial light intensity variation of the incident Gaussian laser beam. On the $z_b = 0$ plane, as shown in Figure 6(b), the photodetector output decreases with increasing $|y_b|$ because of not only the intensity variation of the incident laser beam but also the defocusing of the lens system. As a result, the output variation on this plane is larger than that on the x_b - z_b plane as shown in Figure 6(c). Figure 7 shows the simulation results for the bubble diameter of $100\ \mu\text{m}$. The output characteristics are almost the same as the case of $10\ \mu\text{m}$ except for the absolute value of the output. The photodetector output is normalized by the maximum value in each simulation. Thus, the maximum values are both unity but the absolute maximum value for the $100\ \mu\text{m}$ case is about 10^2 times larger than that of $10\ \mu\text{m}$ case.

Let us define the measurement volume V as the region where the photodetector output has a value larger than $1/e^2$ of its half maximum value as

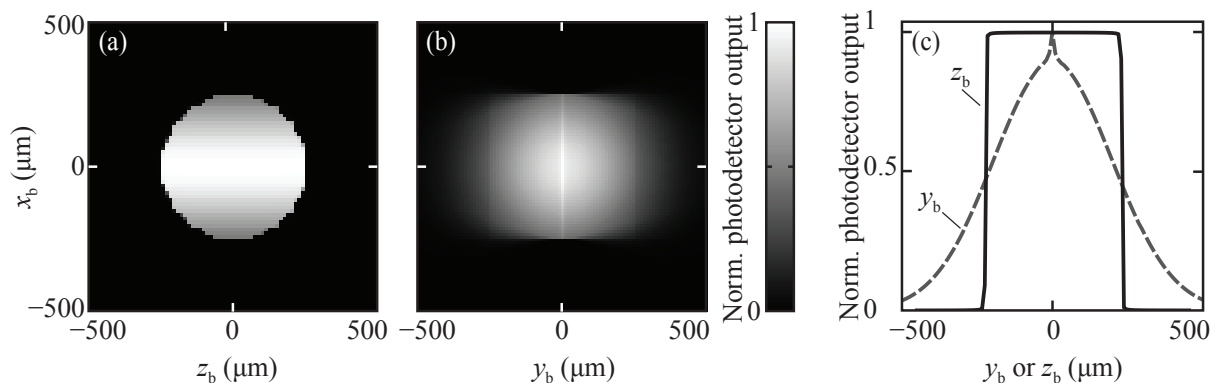


Figure 6 – Bubble position dependence of photodetector output for bubble diameter of $10\ \mu\text{m}$. (a) Output on x_b - z_b plane. (b) Output on x_b - y_b plane. (c) Output along x_b and z_b -axis.

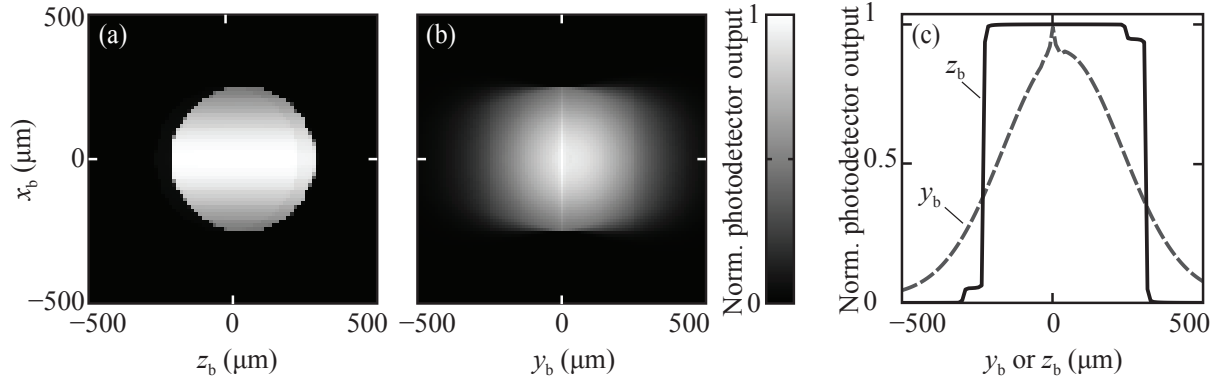


Figure 7 – Bubble position dependence of photodetector output for bubble diameter of 100 μm . (a) Output on x - y plane. (b) Output on x - z plane. (c) Output along x_b and z_b -axis.

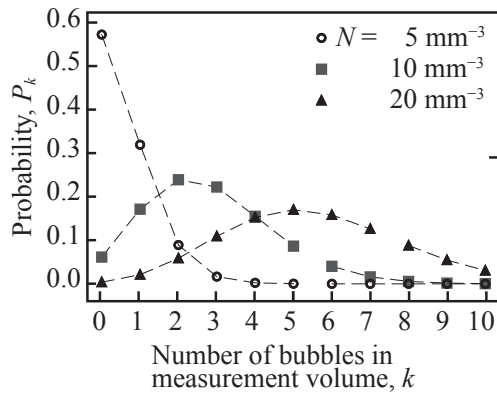


Figure 8 – Probability of existing k bubbles in measurement volume

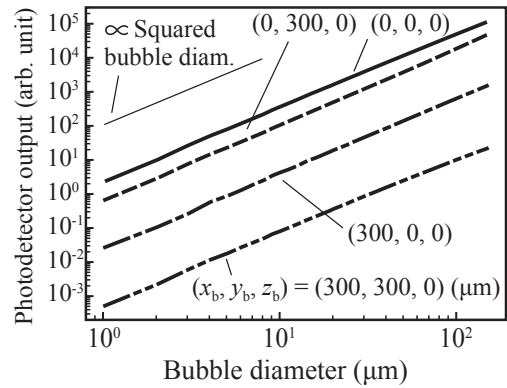


Figure 9 – Relationship between bubble diameter and photodetector output

$$V = \iiint_{O(x_b, z_b, z_b) > \max\{O(x_b, z_b, z_b)\} \exp(-2)} dx dy dz. \quad (18)$$

The measurement volumes calculated from the simulation result for the bubble diameter of 10 and 100 μm are 142.6×10^{-3} and $138.4 \times 10^{-3} \text{ mm}^3$, respectively. These values are almost the same as the simple approximation value $157.0 \times 10^{-3} \text{ mm}^3$ calculated with Eq. 1. The probability of existing k bubbles, whose diameter is 10 μm , in the measurement volume calculated with Eq. 2 is shown in Figure 9 for the bubble number density N of 5, 10, and 20 mm^{-3} . For the bubble number density of 5 mm^{-3} , the probabilities for $k = 0$ and 1 are high. Thus, when the relatively low number density condition, the photodetector output represent the signal from a single bubble.

3.3 Bubble Diameter Dependence of Photodetector Output

The relationship between the photodetector output and the bubble diameter is shown in Figure 9. The plots are for four bubble position and the dashed line showing the slope corresponding to the square of the diameter is also plotted. Although the absolute value decreases with increasing the distance between the origin of the optical system and the bubble position, the photodetector output keeps monotonical increase with the bubble diameter and the square relation with the bubble diameter. Therefore, the radial oscillation of the bubble can be monitored from the output signal.

4. Experimental Results and Discussion

Figures 10(a-i) – 10(c-i) show the typical waveforms of the photodetector output obtained with the above-mentioned setup for the BLT driving power of 6.2, 13.6, and 21.1 W, respectively. The waveforms are lowpass-filtered with cutoff frequency of 1MHz. The several peaks of the waveform observed in Figure 10(a-i) corresponds to the passing of a bubble in the measurement volume. Figure

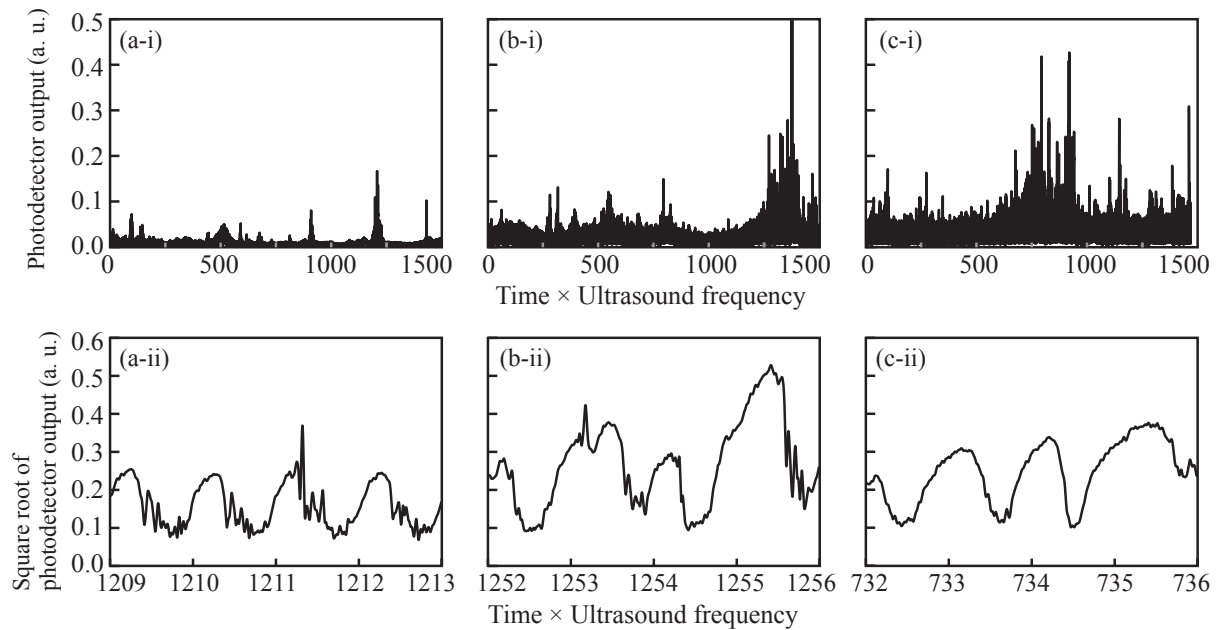


Figure 10 – Experimentally obtained photodetector output. (a) – (c) correspond to BLT driving power of 6.2, 13.6, and 21.1 W, respectively. (ii) is magnified plot of square root of (i).

10(a-ii) shows the enlarged view of the peak around 1200th ultrasound period shown in Figure 10(a-i). The vertical axis shows the square root of the photodetector output to interpret the output to the bubble diameter because of the square relation between the output and the diameter. The bubble diameter vibrates in almost the ultrasound period. The rapid contraction subsequent to the gradual expansion and the bounce after the rapid contraction, which are often observed in the single bubble oscillation (6, 7), are observed. This result may indicate that the waveform is derived from the oscillation of a single bubble in the measurement volume.

The number of peaks and the percentage of the time when the photodetector output has a relatively high value around 0.05 are increasing with increasing the BLT driving power. This is because that the number density of the bubble increases with the BLT driving power and the probability of existing bubbles in the measurement volume increases. In the same manner, the increase of the region with relatively high photodetector output without a clear peak is caused by the increasing of the number of bubbles around the measurement volume, where has relatively low light intensity of the incident beam. Thus, the waveforms without the clear peak may be derived from the scattered light from the many bubbles not from a single bubble. The clear peak is also derived from the sum of the scattered light from the measurement volume and peripheral region, but the waveforms in the clear peak may be dominated by a few bubbles in the measurement volume because the intensity of the incident laser beam in the measurement volume is much higher than that of the peripheral region. Supposing that the output waveform shown in Figures 10(b-ii) and 10(c-ii) is derived from a single bubble, the source of the scattered light may be a relatively large bubble because the rebound has not occurred and these have rectified sinusoidal-like waveform, which is the typical waveform of the large bubble in single bubble oscillation. In the case shown in Figure 10(b-ii), the maximum value of the waveform varied period by period. It may indicate the sub-harmonic oscillation of the bubbles.

5. CONCLUSIONS

A measurement method of oscillation of a bubble in acoustic cavitation employing the laser scattering and the lens system is proposed. The concept and the principle are described and the numerical simulation shows that the method can form a tiny measurement volume and the scattered light from a single bubble, whose intensity is proportional to the bubble diameter, can be obtained with the method. A verification experiment measuring the acoustic cavitation formed under the horn of the BLT shows that the measurement system can obtain the single bubble oscillation-like waveform and the waveform of the bubble varies with the BLT driving power. Thus, we conclude

that the proposed method can measure the oscillation of a single bubble in acoustic cavitation. We will try to the further development of the output signal processing technique and the optimization of the optical system for the quantitative investigation of the bubble oscillation.

ACKNOWLEDGEMENTS

This work was supported by JSPS KAKENHI Grant Number 19K15000.

REFERENCES

1. Choi PK. Sonoluminescence and acoustic cavitation. *Jpn J Appl Phys.* 2017;56:07JA01.
2. Tiong TJ, Chandesa, T, Yap YH. Comparison of sonochemiluminescence images using image analysis techniques and identification of acoustic pressure fields via simulation. *Ultrason Sonochem.* 2017;36:78-87.
3. Panneerselvam S, Mangalaraja RV, Anandan S. Review on the recent improvements in sonochemical and combined sonochemical oxidation processes -- A powerful tool for destruction of environmental contaminants. *Renewable Sustainable Energy Rev.* 2016;55:426-454.
4. Lauterborn W, Bolle H. Experimental investigations of cavitation-bubble collapse in the neighbourhood of a solid boundary. *J Fluid Mech.* 1975;72(2):391-399.
5. Gaitan DF, Crum LA, Church CC, Roy RA. Sonoluminescence and bubble dynamics for a single, stable, cavitation bubble. *J Acoust Soc Am.* 1992;91(6):3166-3183.
6. Kozuka T, Hatanaka S, Yasui K, Tuziuti T, Mitome H. Simultaneous Observation of Motion and Size of a Sonoluminescing Bubble. *Jpn J Appl Phys.* 2002;41:3248-2349.
7. Gompf B, Pecha R. Mie scattering from a sonoluminescing bubble with high spatial and temporal resolution. *Rhys Rev E.* 2000;61(5):5253-5256.
8. Weninger KR, Barber BP, Putterman SJ. Pulsed Mie Scattering of the Collapse of a Sonoluminescing Bubble. *Phys Rev Lett.* 1997;78(9):1799-1802.
9. Yashiro H, Sasaki F, Kakehata M. Measurement of number density of water droplets in aerosol by laser-induced breakdown. *Appl Phys Express.* 2010;3:036601.
10. Hayashi S. Finite angular resolution Mie-scattering measurements of sonoluminescing bubble. *Jpn J Appl Phys.* 1999;38:6562-6563.
11. Lock AJ. Improved Gaussian beam-scattering algorithm. *Appl. Opt.* 1995;34(3):559-570.
12. Kuroyama T. Spatial distribution measurement of acoustic cavitation bubbles by laser backscattering with confocal optics. *Acoust Sci Tech.* 2019;40(4):(in printing).
13. Wilson T. Resolution and optical sectioning in the confocal microscope. *J Microscopy.* 2011;244:113-121.
14. Goodman JW. Introduction to Fourier optics. 4th ed. state, USA:WH Freeman; 2017.